Computational Approaches to Understanding Surface Heat Flow, the Metamorphic Rock Record, and Subduction Geodynamics

by

Buchanan C. Kerswell

A dissertation
submitted in partial fulfillment
of the requirements for the degree of
Doctor of Philosophy in Geosciences
Boise State University

November 2021

© 2021

Buchanan C. Kerswell

ALL RIGHTS RESERVED

BOISE STATE UNIVERSITY GRADUATE COLLEGE

DEFENSE COMMITTEE AND FINAL READING APPROVALS

of the dissertation submitted by

Buchanan C. Kerswell

Dissertation Title: Computational Approaches to Understanding Surface Heat Flow, the Metamorphic Rock Record, and Subduction Geodynamics

Date of Final Oral Examination: August 27, 2021

The following individuals read and discussed the dissertation submitted by student Buchanan C. Kerswell, and they evaluated the student's presentation and response to questions during the final oral examination. They found that the student passed the final oral examination.

Matthew J. Kohn Ph.D.	Chair, Supervisory Committee
C.J. Northrup Ph.D.	Member, Supervisory Committee
H.P. Marshall Ph.D.	Member, Supervisory Committee
Philippe Agard Ph.D.	External Member, Supervisory Committee

The final reading approval of the dissertation was granted by Matthew J. Kohn Ph.D., Chair of the Supervisory Committee. The dissertation was approved by the Graduate College.

DEDICATION

To my mentors, colleagues, friends, and loved ones who take special interests in my life.

This work is yours as much as it is mine.

ACKNOWLEDGMENT

This work was only possible through the efforts of many individuals. My advisor, Dr. Matthew Kohn, deserves special recognition for his contributions, mentorship, and relentless support during the course of my studies. Dr. Taras Gerya and the Geophysical Fluid Dynamics group at the Institut für Geophysik, ETH Zürich, generously offered their high-performance computing resources from the Euler cluster, invaluable instruction, discussion, and support on the numerical modelling methods, and many free meals in Zürich. Additional high-performance computing support from the Borah cluster was provided by the Research Computing Department at Boise State University. Thanks to Dr. D. Hasterok for providing references and guidance on citing the large dataset in chapter three. Special thanks to Dr. Philippe Agard, Dr. Laetitia Le Pourhiet, and graduate students at Sorbonne Université for their incredible expertise and showing me the best of summertime Paris. Thanks to many anonymous reviewers, graduate students, and colleagues for helpful comments on technical aspects of each chapter. My deep appreciation of metamorphic rocks and Alpine geology was formed thanks to outstanding field excursions expertly guided by EFIRE and ZiP graduate students, faculty, and affiliates. Funding for this work was provided by the National Science Foundation grant OIA1545903 awarded to Dr. Matthew Kohn, Dr. Sarah

Penniston-Dorland, and Dr. Maureen Feineman. Datasets and code for reproducing this research are available at https://github.com/buchanankerswell.

ABSTRACT

Pressure-temperature-time (PTt) estimates from high-pressure (HP) metamorphic rocks and global surface heat flow (SHF) rates evidently encode information about pressure-temperature-strain (PTS) fields deep in subduction zones (SZs). Previous work demonstrates the possibility of decoding such geodynamic information by comparing physics-based numerical models with empirical observations of SHF and the metamorphic rock record. However, antithetical interpretations of (non)uniformity with respect to PTS fields are emerging from this line of inquiry. For example, while mechanical coupling depths (CDs) inverted from SHF are narrowly distributed among SZs, maximum pressure-temperature (PT) conditions inverted from exhumed metamorphic rocks are relatively wide-ranging, and yet also uniformly distributed across pressures up to 2.4 GPa. This dissertation scrutinizes (dis)similarities among SZs inferred from large numerical and empirical datasets by applying a variety of computational techniques. First, CDs for 13 modern SZs are predicted after observing coupling in 64 numerical geodynamic simulations. Second, spatial patterns of SHF are assessed in two-dimensions by interpolating thousands of SHF observations near several SZ segments. Third, PTt distributions of over one million markers traced from the previous set of 64 SZ simulations are compared with hundreds of empirical PTt estimates from the rock record to assess the effects of thermo-kinematic boundary conditions (TKBCs) on deep mechanical processing of rock in SZs. These studies conclude the following. Mechanical coupling between plates is primarily controlled by the upper plate lithospheric thickness, with marginal responses to other TKBCs. SHF interpolations show high variance within and among SZ segments, suggesting local, rather than widespread, continuity of PTS fields deep within SZs. Computed marker recovery rates correlate with TKBCs, and are therefore expected to vary among SZs. Finally, computed PTt distributions of markers show patterns consistent with transient, localized recovery from a cooling, serpentinizing plate interface. Together, this work encourages more antireductionist and diversified views of subduction geodynamics until SHF and PTt datasets can more precisely distinguish (dis)similarities in PTS fields within and among SZs. Strategically scaling PTt and SHF datasets in the future will improve computational precision and confidence, and thus will advance subduction zone research.

TABLE OF CONTENTS

Dedication iv

Acknowledgment v

Abstract vii

List of Figures xi

List of Tables xii

List of Abbreviations xiii

List of Symbols xiv

1 Introduction 1

2 Effects of Thermo-kinetic Boundary Conditions on Mechanical Plate Coupling in Subduction Zones 3

- 2.1 Abstract 3
- 2.2 Introduction 4
- 2.3 Numerical modelling methods 7
  - 2.3.1 Initial setup and boundary conditions 8
  - 2.3.2 Calculating geotherms and defining lithospheric thickness 11

3 A Comparison of Heat Flow Interpolations Near Subduction Zones 15

3.1 Abstract 15

References 17

LIST OF FIGURES

2.1 Initial model configuration and boundary conditions 10

2.2 Range of key thermo-kinematic boundary conditions used in numerical experiments 12

LIST OF TABLES

2.1 Rheologic parameters used in numerical experiments 9

2.2 Melting curve constants used in numerical experiments 9

LIST OF ABBREVIATIONS

CD coupling depth

HP high-pressure

PT pressure-temperature

PTS pressure-temperature-strain

PTt pressure-temperature-time

SHF surface heat flow

SZ subduction zone

TKBCs thermo-kinematic boundary conditions

UPT upper plate thickness

LIST OF SYMBOLS

GPa	Gigapascal
K	Kelvin
Ma	*Mega annum* or million-years
Z_{UP}	Upper plate thickness
Z_{cpl}	Mechanical coupling depth
Φ	Thermal parameter
η	viscosity
$\vec{q}$	surface heat flow
$\vec{v}_{conv}$	convergence velocity
$^{\circ}C$	Celcius
km	kilometer
t_{OP}	oceanic plate age

CHAPTER 1:

INTRODUCTION

Keypoints:

- Proxy datasets are key for inference about geodynamics deep in SZs
- Computation leverages large data to infer, build, and test geodynamic models

CHAPTER 2:

EFFECTS OF THERMO-KINETIC BOUNDARY CONDITIONS ON MECHANICAL PLATE COUPLING IN SUBDUCTION ZONES

Keypoints:

- Mechanical coupling responds strongly to upper plate thickness (UPT)
- Inverting surface heat flow (SHF) allows coupling depth (CD) estimation
- Globally consistent UPT would support globally uniform CDs

2.1 Abstract

Deep mechanical coupling between converging plates is a key feature of subduction zone (SZ) geodynamics. Onset of coupling likely corresponds with metamorphic dehydration reactions, and therefore, is dependent on pressure-temperature-strain (PTS) fields within SZs.

The effects of thermo-kinematic boundary conditions (TKBCs) on coupling are considered using two-dimensional numerical models of oceanic-continental convergent margins. The focus is specifically on responses to thermal parameter (Φ) and upper plate thickness (UPT). Coupling is implemented numerically by including experimentally-determined (de)hydration reactions of antigorite and olivine. During the experiments, thermal feedbacks regulating (de)hydration self-consistently within the mantle wedge are observed—stabilizing coupling after ca. 5 Ma. CDs respond strongly to UPT and weakly to Φ. Regression of the results allows coupling depth (CD) estimation for modern SZ segments by inverting UPT from surface heat flow (SHF). The implications for common CDs among SZs are considered, which would require consistent UPT, and thus, globally consistent SHF in the backarc region.

2.2 Introduction

Deep subduction geodynamics strongly depend on the depth where the subducting plate and overlying mantle transition from mechanically decoupled (moving differentially with respect to each other) to mechanically coupled (moving with the same local velocity, Furukawa, 1993; Peacock *et al.*, 1994; Wada *et al.*, 2008). Traction forces drive mantle wedge circulation at the (de)coupling transition, defining a rapid increase in temperature along the top of the subducting plate (Peacock, 1996). Many observations from numerical experiments and SHF infer CDs occurring globally at 70-80 km in modern SZs, essentially independent of other TKBCs including oceanic-plate age (t_{OP}), convergence velocity ($\vec{v}_{conv}$), and subduction geometry (Furukawa, 1993; Wada *et al.*, 2008; Wada & Wang, 2009). It is significant and curious why modern subduction zones appear to achieve similar depths of coupling despite their different physical characteristics.

Notwithstanding, many numerical geodynamic models use CDs of 70-80 *km* as a boundary condition (e.g., Abers *et al.*, 2017; Currie *et al.*, 2004; Syracuse *et al.*, 2010; van Keken *et al.*, 2011, 2018; Wada *et al.*, 2012; Gao & Wang, 2014; Wilson *et al.*, 2014), although not exclusively (e.g. 40-56 *km*, England & Katz, 2010; Peacock, 1996). Similar CDs among SZs is an attractive hypothesis for at least two reasons: 1) it helps explain the relatively narrow range of depths to subducting oceanic-plates beneath volcanic arcs (England *et al.*, 2004; Syracuse & Abers, 2006), as mechanical coupling is expected to be closely associated with the onset of flux melting, and 2) since mechanical coupling is required to detach and recover rocks from the subducting plate (Agard *et al.*, 2016), a common depth of coupling may also help explain why the maximum pressures recorded by subducted oceanic material worldwide is ca. 2.3-2.5 *GPa* (roughly 80 *km*, Agard *et al.*, 2009).

The location and extent of mechanical coupling along the plate interface is implicated in myriad geodynamic phenomena (seismicity, metamorphism, volatile fluxes into the mantle wedge, volcanism, and plate motions, e.g., Čížková & Bina, 2013; Gonzalez *et al.*, 2016; Peacock, 1990, 1991, 1993, 1996; Peacock & Hyndman, 1999; Hacker *et al.*, 2003; van Keken *et al.*, 2011; Grove *et al.*, 2012; Gao & Wang, 2017). Consequently, the mechanics of coupling have been extensively studied and discussed. Coupling fundamentally depends on the strength (η; viscosity) of materials above, within, and below the plate interface. In general, high water fluxes due to compaction and dehydration of clays and other hydrous minerals in the shallow forearc mantle wedge, coupled with increases in PT, form layers of low viscosity sheet silicates—especially talc and serpentine—that inhibit transmission of shear stress from the oceanic-plate to the mantle wedge (Peacock & Hyndman, 1999). The lack of traction along the interface combined with cooling from the subducting plate surface ensures the shallow mantle wedge remains cold and rigid. Experimentally determined flow laws (e.g., Agard *et al.*, 2016), petrologic observations (e.g., Agard *et al.*, 2016), and geophysical observations (e.g., Gao & Wang, 2014; Peacock & Hyndman, 1999) all support the plausibility of this conceptual model of subduction interface behaviour.

This chapter focuses on two fundamental questions: 1) how does mechanical CD respond to TKBCs, and 2) how stable is mechanical CD through time? Two-dimensional numerical geodynamic models of subduction are used to investigate potential correlations between CD, UPT (inverted from backarc heat flow), and Φ. Wada & Wang (2009) previously investigated steady-state CDs by modelling 17 active subduction zones. Among other parameters, their models specify convergence rate, subduction geometry, thermal structure of incoming and overriding plate, and degree of coupling along the subduction interface. Their experiments control for interface rheology and discriminate the best-fit depth based on observed fore-arc heat flow. In the present study, similar TKBCs are specified to simulate the range of modern SZ systems. However, subduction dip angle and, most importantly, interface rheology are regulated self-consistently by evolving PTS fields in a deforming mantle wedge. In other words, CDs in the present study are not a fully determined features, but rather spontaneous model outcomes within the range of specified boundary conditions. As in other previous studies (e.g., Ruh *et al.*, 2015), rheological effects of the dehydration reaction $antigorite \Leftrightarrow olivine + orthopyroxene + H_2O$ are included to drive mechanical coupling by an abrupt viscosity increase with antigorite loss. The position of this reaction along the subduction interface determines the CD.

In this study, subduction is simulated for 64 convergent margins with variable UPT and Φ and mechanical plate coupling is observed. CD responses to Φ and UPT are quantified using multi-variate linear regression. Thermal feedbacks within the system are then visualized in terms of mantle temperature, viscosity, and velocity fields. Lastly, this study discusses how feedbacks stabilize CDs through millions of years of active subduction.

2.3 Numerical modelling methods

The numerical experiments in this study simulate converging oceanic-continental plates, where an ocean basin is being consumed by subduction at a continental margin (Figure 2.1). The initial conditions are modified from previous numerical experiments of active margins (code: `I2VIS`, Sizova *et al.*, 2010; Gorczyk *et al.*, 2007), although plate coupling was not the focus of their studies. Identical material properties (Tables 2.1 & 2.2), rheologic model, and hydration/melt model (see !!!Appendix) as Sizova *et al.* (2010) are used. However, the version of `I2VIS` in this study differs from Sizova *et al.* (2010) in its initial setup, overall dimension, resolution, continental geotherm, dehydration model, and left boundary condition (origin of new oceanic lithosphere). These differences are outlined below. Sixty-four models were constructed with varying convergence rate ($\vec{v}_{conv}$), oceanic-plate age (t_{OP}), and the UPT (Figure 2.2).

2.3.1 Initial setup and boundary conditions

The two-dimensional model is 2000 *km* wide and 300 *km* deep (Figure 2.1). In the model domain, three governing equations of heat transport, motion, and continuity are discretized and solved using a conservative finite-difference with marker-in-cell approach on a fully staggered grid as outlined in Gerya & Yuen (2003). The model resolution is non-uniform with higher resolution (1 *km* x 1 *km*) in a 600 *km* wide area surrounding the contact between the ocean basin and continental margin, then gradually changing to lower resolution towards the model boundaries (5 *km* x 1 *km*, x- and z-directions, respectively). The left and right boundaries are free-slip and thermally insulating (Figure 2.1a, b). The implementation of “sticky” air and water allows for a free topographical surface with a simple linear sedimentation and erosion model. The lower boundary is open to allow for spontaneous oceanic-plate descent and subduction angle (Burg & Gerya, 2005).

Table 2.1: Rheologic parameters used in numerical experiments

Material	Flow Law	h	m	n	A	A_{diff}	A_{disl}	V	V_{diff}	V_{disl}	E	E_{diff}	E_{disl}	σ_{cr}	C	μ_0	μ_1
		$[m]$			$[Pa^n s]$	$[s^{-1}]$	$[s^{-1}]$	$[\frac{J}{Pa \cdot mol}]$	$[\frac{J}{Pa \cdot mol}]$	$[\frac{J}{Pa \cdot mol}]$	$[\frac{J}{mol}]$	$[\frac{J}{mol}]$	$[\frac{J}{mol}]$	$[Pa]$	$[Pa]$		
Felsic sediments	Wet quartzite			2.3	1.97e+17			0.000003			154000			30000	1000000	0.2	0.1
Felsic crust	Wet quartzite			2.3	1.97e+17			0.000003			154000			30000	1000000	0.6	0.3
Oceanic crust	Plag An_{75}			3.2	4.8e+22			0.000008			238000			30000	300000	0.6	0.2
Dry mantle	Dry olivine	0.001	2.5	3.5		8.7e+15	3.5e+22		0.000004	0.00002		300000	540000		1000000	0.6	0.3
Hydrated mantle	Wet olivine	0.001	2.5	3		5.3e+15	2e+18		0.000004	0.00001		240000	430000		1000000	0.6	0.3
Serpentinized mantle	Serpentine			3.8	3.21e+36			0.0000032			8900			3000000	1000000	0.2	0.1
Reference[1]	b, c, d	d	d	b, c, d	b, c	d	d	b, c	d	d	b, c	d	d	b, c	a		

h=grain size, m=grain size exponent, n=stress exponent, A=material constant, V=activation volume, E=activation energy, σ_{cr}=critical stress for dislocation creep, C=compressive strength at P=0, $\mu_{0,1}$=initial and final internal friction coefficient, $\mu_0 = \mu_1 = 0$ for melt-bearing rocks

[1] a=Turcotte & Schubert (2002), b=Ranalli (1995), c=Hilairet et al. (2007), d=Karato & Wu (1993)

Table 2.2: Melting curve constants used in numerical experiments

Material	a[1]	b[1]	c[1]	d[1]	e[1]	f[2]	g[2]	h[2]	i[3]	j[3]
	$[MPa]$	$[K]$	$[MPa]$	$[MPa]$	$[MPa]^2$	$[K]$	$[MPa]^{-1}$	$[MPa]^{-2}$	$[K]$	$[MPa]^{-1}$
Felsic sediments	1200	889	17900	54	20200	831	0.0600		1262	0.009
Felsic crust	1200	889	17900	54	20200	831	0.0600		1262	0.009
Oceanic Crust	1600	973	704000	354	77800000	935	0.0035	0.000062	1423	0.105
Dry mantle						1394	0.1330	-0.000051	2073	0.114
Hydrated mantle	2400	1240	49800	323			127000.0000	0.000035	2073	0.114
Serpentinized mantle	2400	1240	49800	323			127000.0000	0.000035	2073	0.114

After phase diagrams from Schmidt & Poli (1998)

[1] $T_{solidus}(P) = b + \frac{c}{(P+d)} + \frac{e}{(P+d)^2}$ at $P < a$

[2] $T_{solidus}(P) = f + gP + hP^2$ at $P \geq a$

[3] $T_{liquidus}(P) = i + jP$

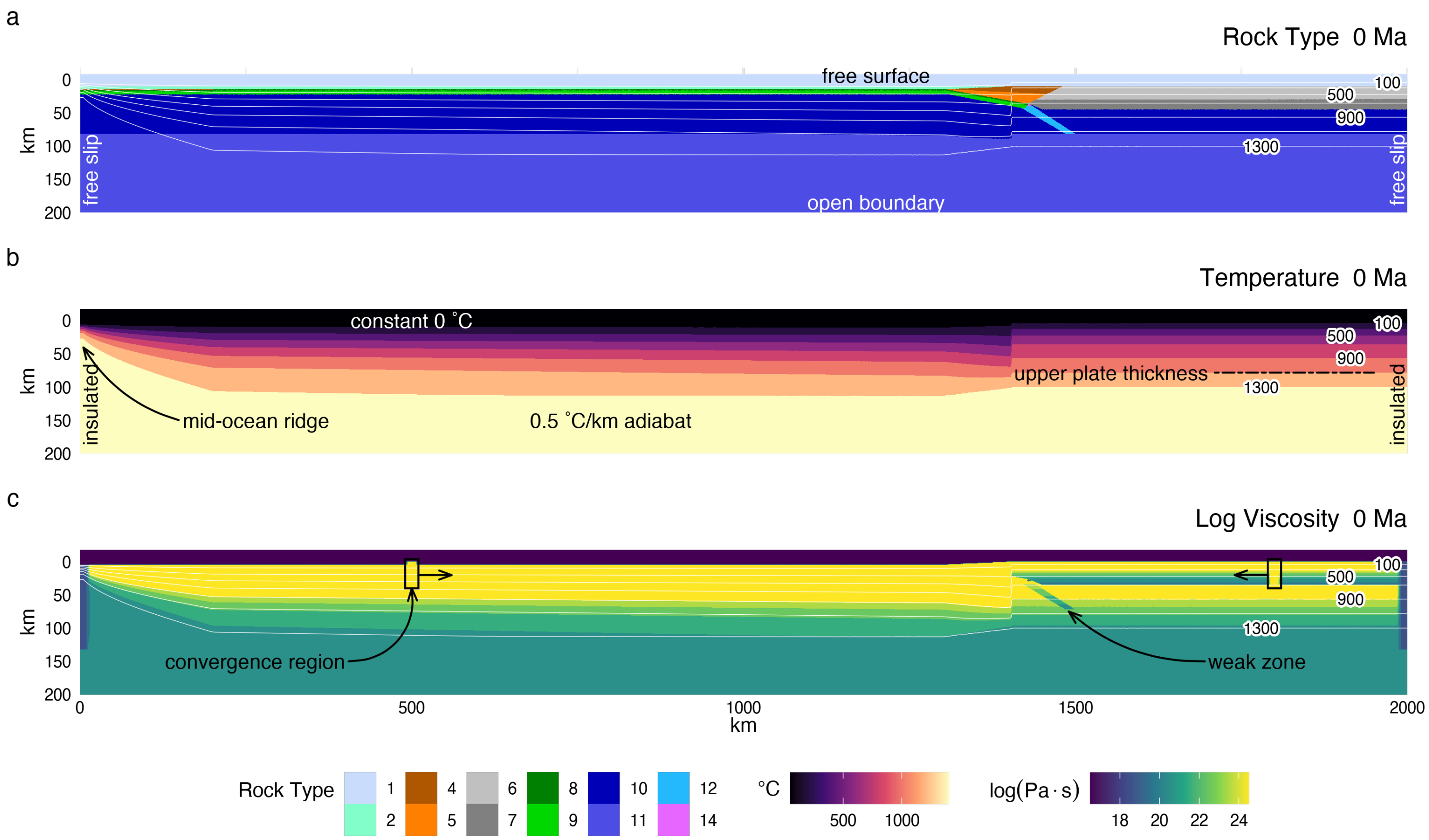
a
Rock Type 0 Ma
free surface
free slip
open boundary
b
Temperature 0 Ma
constant 0 ˚C
insulated
mid-ocean ridge
0.5 ˚C/km adiabat
upper plate thickness
c
Log Viscosity 0 Ma
convergence region
weak zone
100
500
900
1300
km
0
50
100
150
200
0
500
1000
1500
2000
Rock Type
1
2
4
5
6
7
8
9
10
11
12
14
°C
500
1000
log(Pa · s)
18
20
22
24

Figure 2.1: Initial model configuration and boundary conditions. (a) A free sedimentation/erosion boundary at the surface is maintained by implementing a layer of "sticky" air and water, and an infinite-like open boundary at the bottom allows for spontaneous oceanic-plate descent and subduction angle. The left and right boundaries are free slip and insulating. The initial material distribution includes 7 km of oceanic crust (2 km basalt, 5 km gabbro), 1 km of oceanic sediments, and 35 km of continental crust, thinning ocean-ward. (b) Oceanic lithosphere is continually created at the left boundary. The oceanic geotherm is calculated using a half-space cooling model and the continental geotherm is calculated using a one-dimensional steady-state conductive cooling model to 1300 $^{\circ}C$. The base of the mechanical lithosphere (Z_{UP}) is defined by visualizing viscosity and generally coincides with the 1100 $^{\circ}C$ isotherm. (c) The oceanic crust is bent under loading from passive margin sediments, and a weak zone extends from the deflected oceanic crust, through the lithosphere, to help induce subduction. Convergence velocities are imposed at stationary, high-viscosity regions far from the trench. Rock type colors are: [1] air, [2] water, [4,5] sediments, [6,7] felsic crust, [8] basalt, [9] gabbro, [10,11] dry mantle, [12] hydrated mantle, [14] serpentinized mantle.

A horizontal convergence force is applied to both plates in a rectangular region far from the continental margin (Figure 2.1c). An initial weak layer cutting the lithosphere permits subduction to initiate. The high-viscosity ($\eta = 10^{25}\ Pa \cdot s$) rectangular convergence regions apply constant horizontal velocities without deforming the lithosphere. The subduction angle is governed by the free-motion of the subducting plate. Similarly, subduction velocity can vary with time in response to extension or shortening of the overriding plate. Therefore, the thermal parameter (Φ) is calculated in this study as the product of the horizontal convergence velocity ($\vec{v}_{conv}$) and the oceanic-plate age (t_{OP}, c.f. McKenzie, 1969). For convenience and consistency with the literature, this study presents Φ as $\Phi/100$ (Figure 2.2a).

2.3.2 Calculating geotherms and defining lithospheric thickness

The oceanic crust is modeled as 1 km of sediment cover overlying 2 km of basalt and 5 km of gabbro (Figure 2.1a). Oceanic lithosphere is continually made at a pseudo-mid-ocean ridge at the left boundary of the model (Figure 2.1b). An enhanced vertical cooling condition is applied at 200 km from left boundary to adjust for the proper oceanic-plate age, and therefore its lithospheric thickness as it enters the trench (Agrusta *et al.*, 2013). Plate ages from 32.6 to 110 Ma and convergence velocities from 40 to 100 km/Ma are used in this study (Figure 2.2a). This range of parameters broadly reflects the middle-range of the modern global subduction system (Syracuse & Abers, 2006).

Initial continental geotherms are determined by solving the heat flow equation in one-dimension to 1300 $^{\circ}C$ (Figure 2.2b). This study assumes a fixed temperature of 0 $^{\circ}C$ at

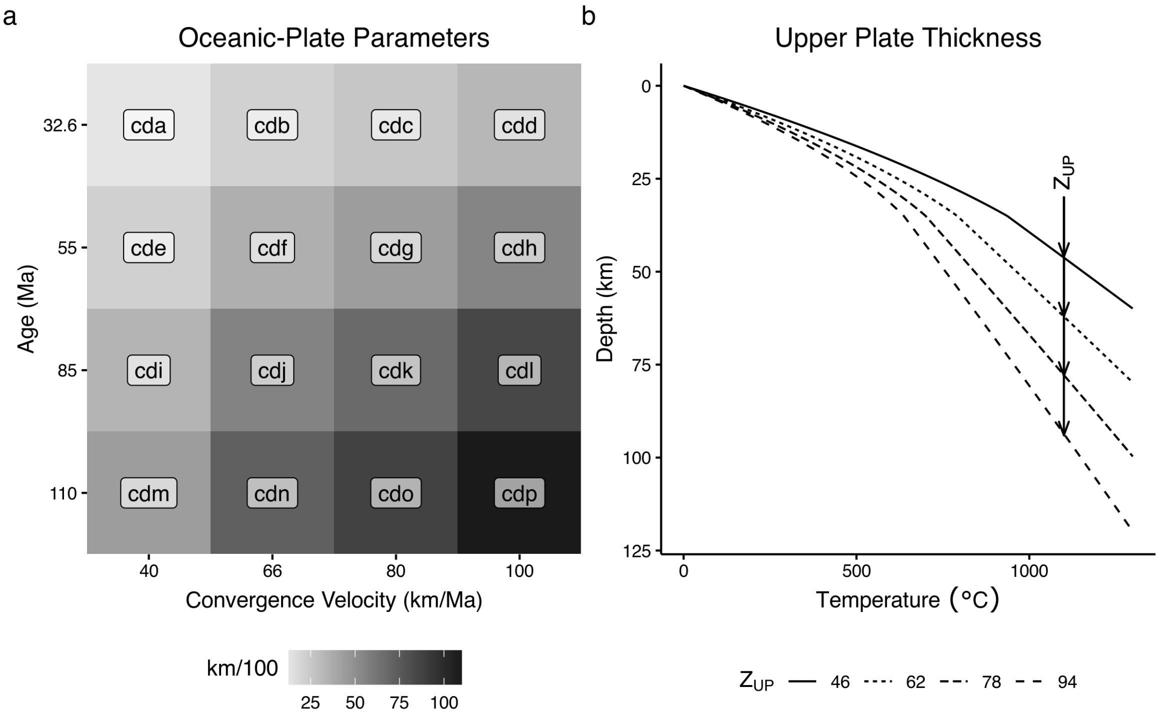

Figure 2.2: Range of key thermo-kinematic boundary conditions used in numerical experiments. (a) Modelled thermal parameters (grayscale) range from 13 to 110 $km/100$ and broadly reflect the distribution of oceanic-plate ages and convergence velocities in modern subduction zones. Model names include the prefix "cd" for "coupling depth" with increasing alphabetic suffixes. Note that neither axes are continuous. (b) Upper plate thickness (Z_{UP}) is defined by a range of continental geotherms. Geotherms were constructed using a one-dimensional steady-state conductive cooling model with $T(z=0)$ = 0 $^\circ C$ and $\vec{q}(z=0)$ = 59, 63, 69, 79 mW/m^2, and constant radiogenic heating of 1.0 $\mu W/m^3$ for a 35 km-thick crust and 0.022 $\mu W/m^3$ for the mantle. The continental geotherms are calculated up to 1300 °C, with a 0.5 $^\circ C/km$ gradient (the mantle adiabat) for higher temperatures.

the surface, constant radiogenic heating of 1 $\mu W/m^3$ in the 35 *km*-thick continental crust, 0.022 $\mu W/m^3$ in the mantle, with thermal conductivities of 2.3 W/mK and 3.0 W/mK for the continental crust and mantle, respectively. Above, 1300 $^\circ C$, temperature is assumed to increase by 0.5 $^\circ C/km$ (the mantle adiabat).

Many studies define the base of the continental lithosphere at the 1300 $^\circ C$ isotherm, but it can be determined directly by visualizing viscosity and strain rate as the model progresses. The mechanical base of the lithosphere (Z_{UP}) in the models generally occurs at the 1100 $^\circ C$ isotherm—characterized by a rapid decrease in viscosity and increase in strain rate (Figures **??**, **??**, **??**). As such, this study considers the oceanic and continental lithosphere as mechanical layers defined by viscosity, rather than defined merely by temperature. The range of Z_{UP} corresponds to backarc surface heat flow of 59, 63, 69, and 79 mW/m^2.

CHAPTER 3:

A COMPARISON OF HEAT FLOW INTERPOLATIONS NEAR SUBDUCTION ZONES

Keypoints:

- Inconsistent spatial patterns characterize heat flow near subduction zones
- Heat flow investigations favour 2D interpolations over 1D transects
- Scaling datasets and new interpolation schema will advance SZ research

3.1 Abstract

Heat fluxing through the Earth's surface provides indirect observations of pressure-temperature-strain (PTS) fields deep in SZs. Global heat flow databases, therefore, are invaluable for generating and testing belief about SZ geodynamics. Investigating surface heat flow (SHF) in two-dimensions by interpolation, rather than in one-dimension by

projection, arguably forms better interpretations about spatial continuity of deep processes. Direct comparisons of interpolations based on the First (spatial continuity) and Third (similarity) Laws of Geography applied to the most updated global heat flow database. Inconsistent spatial patterns of SHF near SZs are observed in magnitude and variance, regardless of interpolation method. The implications include discontinuous PTS fields at depth, countering hypotheses of commonly thin upper plate lithospheres and mechanical CDs among subduction zones. Strategic scaling of SHF datasets will improve interpolation precision and confidence—leading to better tools for distinguishing differences within and among SZs. New data acquisition and composite interpolation schema are proposed as avenues for future SZ research.

REFERENCES

Abers, G. A., van Keken, P. E., & Hacker, B. R. 2017. The cold and relatively dry nature of mantle forearcs in subduction zones. *Nature Geoscience*, **10**(5), 333–337.

Agard, P., Yamato, P., Jolivet, L., & Burov, E. 2009. Exhumation of oceanic blueschists and eclogites in subduction zones: Timing and mechanisms. *Earth-Science Reviews*, **92**(1-2), 53–79.

Agard, P., Yamato, P., Soret, M., Prigent, C., Guillot, S., Plunder, A., Dubacq, B., Chauvet, A., & Monié, P. 2016. Plate interface rheological switches during subduction infancy: Control on slab penetration and metamorphic sole formation. *Earth and Planetary Science Letters*, **451**, 208–220.

Agrusta, R., Arcay, D., Tommasi, A., Davaille, A., Ribe, N., & Gerya, T. 2013. Small-scale convection in a plume-fed low-viscosity layer beneath a moving plate. *Geophysical Journal International*, **194**(2), 591–610.

Burg, J. P., & Gerya, T. 2005. The role of viscous heating in Barrovian metamorphism of collisional orogens: thermomechanical models and application to the Lepontine Dome in the Central Alps. *Journal of Metamorphic Geology*, **23**(2), 75–95.

Čížková, H., & Bina, C. R. 2013. Effects of mantle and subduction-interface rheologies on slab stagnation and trench rollback. *Earth and Planetary Science Letters*, **379**, 95–103.

Currie, C. A., Wang, K., Hyndman, R. D., & He, J. 2004. The thermal effects of steady-state slab-driven mantle flow above a subducting plate: The Cascadia subduction zone and backarc. *Earth and Planetary Science Letters*, **223**(1-2), 35–48.

England, P., & Katz, R. F. 2010. Melting above the anhydrous solidus controls the location of volcanic arcs. *Nature*, **467**(7316), 700–703.

England, P., Engdahl, R., & Thatcher, W. 2004. Systematic variation in the depths of slabs beneath arc volcanoes. *Geophysical Journal International*, **156**(2), 377–408.

Furukawa, Y. 1993. Magmatic Processes Under Arcs and Formation of the Volcanic Front. *Journal of Geophysical Research*, **98**, 8309–8319.

Gao, X., & Wang, K. 2014. Strength of stick-slip and creeping subduction megathrusts from heat flow observations. *Science*, **345**(6200), 1038–1041.

Gao, X., & Wang, K. 2017. Rheological separation of the megathrust seismogenic zone and episodic tremor and slip. *Nature*, **543**(7645), 416–419.

Gerya, T., & Yuen, D. A. 2003. Characteristics-based marker-in-cell method with conservative finite-differences schemes for modeling geological flows with strongly variable transport properties. *Physics of the Earth and Planetary Interiors*, **140**(4), 293–318.

Gonzalez, Christopher M, Gorczyk, Weronika, & Gerya, TV. 2016. Decarbonation of subducting slabs: Insight from petrological–thermomechanical modeling. *Gondwana Research*, **36**, 314–332.

Gorczyk, W., Willner, A. P., Gerya, T., Connolly, J. A.D., & Burg, J. P. 2007. Physical controls of magmatic productivity at Pacific-type convergent margins: Numerical modelling. *Physics of the Earth and Planetary Interiors*, **163**(1-4), 209–232.

Grove, T. L., Till, C. B., & Krawczynski, M. J. 2012. The Role of H 2 O in Subduction Zone Magmatism. *Annual Review of Earth and Planetary Sciences*, **40**(1), 413–439.

Hacker, B. R., Peacock, S. M., Abers, G. A., & Holloway, S. D. 2003. Subduction factory 2. Are intermediate-depth earthquakes in subducting slabs linked to metamorphic dehydration reactions? *Journal of Geophysical Research: Solid Earth*, **108**(B1).

McKenzie, D. P. 1969. Speculations on the Consequences and Causes of Plate Motions. *Geophysical Journal International*, **18**(1), 1–32.

Peacock, S. M. 1990. Fluid processes in subduction zones. *Science*, **248**(4953), 329–337.

Peacock, S. M. 1991. Numerical simulation of subduction zone pressure-temperature-time paths: constraints on fluid production and arc magmatism. *Philosophical Transactions of the Royal Society of London. Series A: Physical and Engineering Sciences*, **335**(1638), 341–353.

Peacock, S. M. 1993. The importance of blueschist → eclogite dehydration reactions in subducting oceanic crust. *Geological Society of America Bulletin*, **105**(5), 684–694.

Peacock, S. M. 1996. Thermal and petrologic structure of subduction zones. *Subduction: top to bottom*, **96**, 119–133.

Peacock, S. M., & Hyndman, R. D. 1999. Hydrous minerals in the mantle wedge and the maximum depth of subduction thrust earthquakes. *Geophysical Research Letters*, **26**(No. 16), 2517–2520.

Peacock, S. M., Rushmer, T., & Thompson, A. B. 1994. Partial melting of subducting oceanic crust. *Earth and planetary science letters*, **121**(1-2), 227–244.

Ruh, J. B., Le Pourhiet, L., Agard, P., Burov, E., & Gerya, T. 2015. Tectonic slicing of subducting oceanic crust along plate interfaces: Numerical modeling. *Geochemistry, Geophysics, Geosystems*, **16**(10), 3505–3531.

Sizova, E., Gerya, T., Brown, M., & Perchuk, L. L. 2010. Subduction styles in the Precambrian: Insight from numerical experiments. *Lithos*, **116**(3-4), 209–229.

Syracuse, E. M., & Abers, G. A. 2006. Global compilation of variations in slab depth beneath arc volcanoes and implications. *Geochemistry, Geophysics, Geosystems*, **7**(5).

Syracuse, E. M., van Keken, P. E., Abers, G. A., Suetsugu, D., Bina, C. R., Inoue, T., Wiens, D., & Jellinek, M. 2010. The global range of subduction zone thermal models. *Physics of the Earth and Planetary Interiors*, **183**(1-2), 73–90.

van Keken, P. E., Hacker, B. R., Syracuse, E. M., & Abers, G. A. 2011. Subduction factory: 4. Depth-dependent flux of H 2 O from subducting slabs worldwide. *Journal of Geophysical Research*, **116**(B1), B01401.

van Keken, P. E., Wada, I., Abers, G. A., Hacker, B. R., & Wang, K. 2018. Mafic High-Pressure Rocks Are Preferentially Exhumed From Warm Subduction Settings. *Geochemistry, Geophysics, Geosystems*, **19**(9), 2934–2961.

Wada, I., & Wang, K. 2009. Common depth of slab-mantle decoupling: Reconciling diversity and uniformity of subduction zones. *Geochemistry, Geophysics, Geosystems*, **10**(10), n/a–n/a.

Wada, I., Wang, K., He, J., & Hyndman, R. D. 2008. Weakening of the subduction interface and its effects on surface heat flow, slab dehydration, and mantle wedge serpentinization. *Journal of Geophysical Research: Solid Earth*, **113**(4), 1–15.

Wada, I., Behn, M. D., & Shaw, A. M. 2012. Effects of heterogeneous hydration in the incoming plate, slab rehydration, and mantle wedge hydration on slab-derived H 2O flux in subduction zones. *Earth and Planetary Science Letters*, **353-354**, 60–71.

Wilson, C. R., Spiegelman, M., van Keken, P. E., & Hacker, B. R. 2014. Fluid flow in subduction zones: The role of solid rheology and compaction pressure. *Earth and Planetary Science Letters*, **401**, 261–274.